

CHEMISTRY

A European Journal



Accepted Article

Title: Self-assembly of Fluorescent Dehydroberberine Enhances Mitochondria-Dependent Antitumor Efficacy

Authors: Ruibing An, Zhanni Gu, Haifeng Sun, Yuxuan Hu, Runqi Yan, Deju Ye, and Hong Liu

This manuscript has been accepted after peer review and appears as an Accepted Article online prior to editing, proofing, and formal publication of the final Version of Record (VoR). This work is currently citable by using the Digital Object Identifier (DOI) given below. The VoR will be published online in Early View as soon as possible and may be different to this Accepted Article as a result of editing. Readers should obtain the VoR from the journal website shown below when it is published to ensure accuracy of information. The authors are responsible for the content of this Accepted Article.

To be cited as: *Chem. Eur. J.* 10.1002/chem.201801112

Link to VoR: <http://dx.doi.org/10.1002/chem.201801112>

Supported by
ACES

WILEY-VCH

Self-assembly of Fluorescent Dehydroberberine Enhances Mitochondria-Dependent Antitumor Efficacy

Ruibing An⁺,^[a] Zhanni Gu⁺,^[b] Haifeng Sun⁺,^[b] Yuxuan Hu,^[a] Runqi Yan,^[a] Deju Ye,^{*[a]} and Hong Liu^{*[b]}

Abstract: Selective imaging and inducing mitochondrial dysfunction in tumor cells using mitochondria-targeting probes has become as a promising approach for cancer diagnosis and therapy. Here, we report the design of a fluorescent berberine analog, dehydroberberine (DH-BBR), as a new mitochondria-targeting probe capable of self-assembling into monodisperse organic nanoparticles (DTNPs) upon integration with a lipophilic counter anion, allowing for enhanced fluorescence imaging and treatment of tumors in living mice. X-ray crystallography revealed that the self-assembly process was attributed to a synergy of different molecular interactions, including π - π stacking, $O\cdots\pi$ interaction and electrostatic interaction between DH-BBR and counter anions. We demonstrated that DTNPs could efficiently enter into tumor tissue following intravenous injection and enhance mitochondrial delivery of DH-BBR via an electrostatic interaction driven anion exchange process. Selective accumulation in the mitochondria capable of emitting strong fluorescence and causing mitochondrial dysfunction was achieved, enabling efficient inhibition of tumor growth in living mice. This study demonstrates promise for applying lipophilic anions to control molecular self-assembly and tune antitumor activity of mitochondria-targeting probes, which can facilitate to improve cancer treatment *in vivo*.

Introduction

Self-assembly of small molecules into nanoarchitectures has emerged as a promising approach to build functional nanomaterials capable of tuning imaging signals,^[1] controlling drug delivery,^[2] and improving therapeutic efficacy.^[3] Tremendous efforts have been made to develop small molecule compounds, including amino acids,^[4] peptides,^[5] and other organic compounds,^[6] with the propensity for self-assembly into organic nanostructures by different intermolecular interactions (e.g., π - π stacking, hydrophobic interactions, ionic attraction, and hydrogen bond). These organic assemblies have the advantages of structural diversity, high biodegradability and tunable functionality, offering wide applications in biology and medicine, such as molecular imaging of enzyme activity,^[1b, 7] tuning antitumor

activity,^[8] and regulating cellular process.^[9] In addition, they can generally use the enhanced permeation and retention (EPR) effect to facilitate the delivery into tumors, ultimately improving the imaging and treatment of tumors *in vivo*.^[10]

Recently, mitochondria-targeting theranostic probes that enable selective imaging and induction of mitochondrial dysfunction have attracted increased attention to advance cancer therapy.^[11] These probes generally use delocalized lipophilic cations (DLCs) to trigger selective delivery of imaging and therapeutic moieties into mitochondria.^[12] One of the most used DLCs is triphenylphosphonium (TPP), which is directly conjugated to the imaging and antitumor cargos, affording TPP-based mitochondria-targeting theranostic probes capable of imaging and killing cancer cells.^[13] Another intriguing approach is the direct use of DLCs-based organic fluorophores (e.g., rhodamine, coumarin) to build mitochondria-targeting theranostic probes through covalently coupling with an antitumor drug.^[13-14] In spite of encouraging results have been demonstrated, both of these two kinds of probes require tedious chemical conjugation of either TPP or DLCs-based fluorophore with the drug, which may interrupt the interactions between the drugs and the molecular targets in cancer cells, potentially reducing the antitumor efficacy.^[15] Therefore, the development of new small molecule DLCs-based compounds with their structure-inherent abilities of mitochondria-targeting, fluorescence imaging and inducing mitochondrial dysfunction without additional chemical conjugation could offer an alternative approach to enhance the mitochondria-dependent antitumor efficacy.

As a natural isoquinoline alkaloid, berberine (BBR) is a widely used traditional Chinese medicine for the treatment of many diseases, such as diabetes, cardiovascular disease, hyperlipemia, and inflammation.^[16] BBR has a cationic structure, which has also been used as a DLCs-based compound capable of targeting to mitochondria, emitting weak green fluorescence and inducing mitochondrial dysfunction in tumor cells.^[17] However, the potency against tumor cells is not very efficient,^[16b] substantially limiting its application as an antitumor drug. Moreover, although BBR contains a multi-aromatic ring structure for emitting fluorescence, the fluorescence quantum yield in aqueous solution (0.0021) is too low for cancer imaging, presumably because of its partial π -conjugated structure (Figure 1a). Thus, the direct application of BBR as a mitochondria-targeting probe for fluorescence imaging and treatment of tumors is very limited. There is still lack of studies to design BBR analogues as efficient mitochondria-targeting probes with improved fluorescence property and antitumor activity.

Herein, we report the design of a new BBR analog, dehydroberberine (DH-BBR, Figure 1a), as a new mitochondria-targeting probe for fluorescence imaging and treatment of tumors *in vivo*. We showed that DH-BBR contains a planar and full π -conjugated multi-ring structure, substantially improving the fluorescence properties and cytotoxicity toward cancer cells compared to that of BBR. The subsequent incorporation of a lipophilic anion tetraphenylborate (TPB) with DH-BBR to trigger

[a] R. An, Y. Hu, R. Yan, Pro. D. Ye
State Key Laboratory of Analytical Chemistry for Life Science,
School of Chemistry and Chemical Engineering, Nanjing University,
Nanjing, 210023, China.

E-mail: dejuye@nju.edu.cn

[b] Z. Gu, Dr. H. Sun, Pro. H. Liu
State key Laboratory of Drug Research and Key Laboratory of
Receptor Research, Shanghai Institute of Materia Medica, Chinese
Academy of Sciences, 555 Zu Chong Zhi Road, Shanghai 201203,
China.

E-mail: hliu@simm.ac.cn

[+] These authors contributed equally to this work.
Supporting information for this article is given via a link at the end of
the document.

FULL PAPER

efficient molecular self-assembly into mono-dispersed nanoparticles (DTNPs) was further demonstrated, which could significantly enhance the delivery of fluorescent DH-BBR into mitochondria of tumor cells, producing much stronger mitochondrial fluorescence than that of DH-BBR. Moreover, DTNPs also showed enhanced cytotoxicity against tumor cells over normal cells via a mitochondria-dependent apoptosis pathway, allowing for efficient inhibition of tumor growth without obvious side effects *in vivo*. This study has demonstrated the great potential of using self-assembly approach to engineer mitochondria-targeting small molecules for improved cancer imaging and therapy.

Results and Discussion

Figure 1a shows the molecular structure of fluorescent mitochondria-targeting compound DH-BBR and the general procedure for the preparation of DTNPs using the lipophilic anion-driven self-assembly approach. DH-BBR is designed to possess a full π -conjugated four-ring structure in relative to BBR, contributing to a longer fluorescence emission wavelength and higher fluorescence quantum yield for tumor cell imaging. Moreover, DH-BBR also possesses a planar structure, which can provide strong molecular interactions (e.g., π - π stacking) to trigger efficient self-assembly into DTNPs. Figure 1b illustrates the mechanism of action by which DTNPs selectively interact with tumor cells via a proposed electrostatic interaction driven anion exchange process. Upon delivery into tumor tissue via the EPR effect, the tumor cell membranes, which are full of negative charges, can trigger DTNPs degradation, liberating the free DH-BBR·TPB ion-pair near the membrane. Subsequent anion exchange between TPB⁻ in the ion-pair and anions on the cell membrane can facilitate cation DH-BBR⁺ entry into cells, while the anion TPB⁻ is blocked extracellularly due to the repulsion interactions. After entering into tumor cells, the DLCs feature of DH-BBR⁺ can prompt their accumulation in the mitochondria, leading to mitochondrial dysfunction and release of cytochrome c (cyt c) into the cytosol. This subsequently activates caspase-3, triggers cell apoptosis, and ultimately induces cell death. Normal cell membranes are less negative than those of tumor cells^[18]; therefore, uptake into normal cells through the proposed electrostatic interaction-driven anion exchange process is reduced, thus exerting weak cytotoxicity. Hence, DTNPs show enhanced and selective cytotoxicity toward tumor cells.

We first synthesized DH-BBR according to the approach outlined in Scheme S1. Owing to the formation of a prolonged π -conjugated coplanar structure, DH-BBR showed bathochromic shifts of UV-Vis absorption ($\lambda_{\text{abs}} = 453 \text{ nm}$) and fluorescence emission ($\lambda_{\text{em}} = 578 \text{ nm}$) relative to that of BBR ($\lambda_{\text{abs}}/\lambda_{\text{em}} = 423/548 \text{ nm}$) in phosphate-buffered saline (PBS) buffer (pH 7.4) (Table S1). More importantly, DH-BBR also showed a significantly higher fluorescence quantum yield ($\Phi_f = 0.15$) than that of BBR (0.0021) in PBS buffer, emitting much higher fluorescence in tumor cells (Figure S1). Subsequent colocalization studies with Mito-tracker or Lyso-tracker demonstrated that DH-BBR accumulated mainly in the mitochondria of HeLa cells (Figure S2), suggesting that the

DLC characteristic of DH-BBR could promote mitochondrial accumulation. We further compared the cytotoxicity of DH-BBR and BBR against both HeLa and MDA-MB-231 tumor cells using the 3-(4,5-dimethylthiazol-2-yl)-2,5-diphenyltetrazolium bromide (MTT) assay. The results showed that DH-BBR exhibited higher cytotoxicity than BBR, with an IC_{50} value of ~ 22.14 and $\sim 32.87 \mu\text{M}$ against HeLa and MDA-MB-231 cells, respectively. In contrast, more than 50% cells were still alive after incubation with $50 \mu\text{M}$ BBR for 48 h (Figure S3). These results demonstrated that DH-BBR was a more appropriate mitochondria-targeting probe than BBR in terms of enhanced fluorescence properties and cytotoxicity.

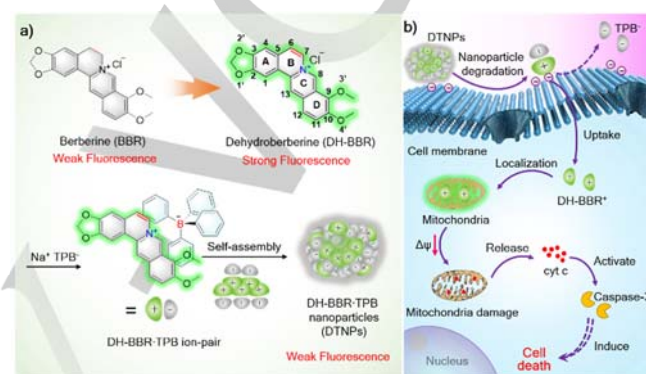


Figure 1. General design of lipophilic anion-driven self-assembly of mitochondria targeting fluorescent cation DH-BBR for enhanced cancer treatment. (a) The chemical structure of BBR, DH-BBR and the general procedure to form DTNPs through self-assembly of DH-BBR·TPB ion-pair. (b) Illustration of the mechanism of DTNPs selectively interact with tumor cells to enhance cellular uptake and cytotoxicity via a mitochondria-dependent apoptosis process.

We then prepared the organic ion-pair DH-BBR·TPB, using the ion-exchange approach shown in Scheme S2. As expected, DH-BBR·TPB showed an increased partition coefficient ($\text{Log } P = 2.75$) compared to that of either DH-BBR⁺Cl⁻ (-0.70) or BBR⁺Cl⁻ (-1.71) (Table S2). This increased lipophilicity could help DH-BBR·TPB to self-assemble into DTNPs in aqueous solution. Dynamic light scattering (DLS) analysis revealed the presence of mono-dispersed nanoparticles in water, with a mean hydrodynamic size of $\sim 110 \text{ nm}$ (Figure 2a). This was also verified by both transmission electron microscopy (TEM) and atomic force microscopy (AFM) analysis, showing spherical nanoparticles with an average diameter of $\sim 100 \text{ nm}$ (Figures. 2b & c). In contrast, neither DH-BBR⁺Cl⁻ nor Na⁺TPB⁻ could self-assemble into nanoparticles under the same conditions (Figure S4), suggesting that the combination of cation DH-BBR⁺ and lipophilic anion TPB⁻ is essential to form DTNPs.

To clarify the molecular interactions for the self-assembly, a single crystal structure of DH-BBR·TPB was obtained using X-ray crystallography. A perspective view of DH-BBR·TPB is shown in Figure 2d, and the crystal refinement data are summarized in Table S3. The crystal packing structure of DH-BBR·TPB shows two different stacking modes between DH-BBR cations along axis b (Figure 2e & Figure S5). In mode one, the two DH-BBR cations

FULL PAPER

take an offset π - π stacking between the four aromatic rings from each other, with an interplanar distance of 3.38 Å (red dash lines, Figure 2e). Each cation adopts an antiparallel arrangement that can reduce the steric/electrostatic repulsions. In mode two, the two DH-BBR cations take a head-to-head stacking between the aromatic ring A and 1,3-dioxolo ring from each other, offering two strong O $\cdots\pi$ interactions ($O2\cdots\pi = 3.31$ Å, green dashed lines). These two different, strong intermolecular interactions promote DH-BBR cations to pack together closely, forming supramolecular chains. These are further connected by adjacent lipophilic TPB anions through electrostatic interactions between N⁺ in DH-BBR⁺ and B⁻ in TPB⁻ (blue dashed lines, Figure 2f). Moreover, slipped π - π stacking between one phenyl ring of TPB⁻ and two aromatic rings of DH-BBR⁺ (rings C and D) also occurs (magenta dashed lines, interplanar distance of 3.78 Å), which can provide additional molecular interactions to connect DH-BBR cations together (Figure S6). As such, DH-BBR⁺·TPB⁻ is prone to self-assemble into nanoparticles through the synergy of π - π stacking, O $\cdots\pi$ interaction and electrostatic interaction.

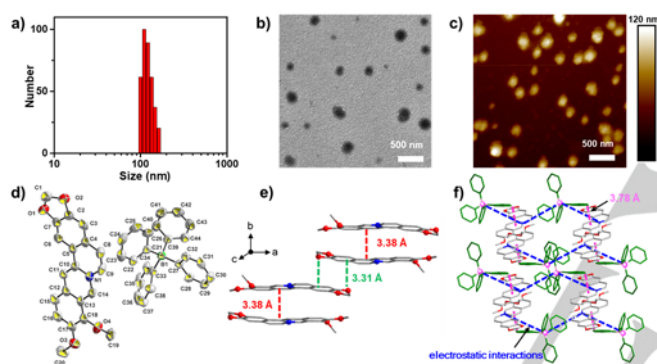


Figure 2. Nanocharacterization of DTNPs. (a) DLS analysis, (b) TEM and (c) AFM images of DTNPs (20 μ M) in H₂O. (d) Single crystal structure of DH-BBR·TPB. (e) The packing structure of DH-BBR cations along axis b. Red dash lines indicate the offset π - π stacking between two adjacent DH-BBR cations, and green dash lines indicate the O $\cdots\pi$ interactions between another two DH-BBR. The TPB⁻ anions are omitted for clarity. (f) The packing structure of DH-BBR·TPB shows the presence of both slipped π - π stacking (magenta dash lines) and electrostatic interactions (blue dash lines) between DH-BBR⁺ and TPB⁻. The phenyl rings in TPB⁻ are shown green, and the B atoms are shown magenta. All H atoms in the structures were omitted for clarity.

The self-assembly of DH-BBR·TPB into DTNPs in PBS buffer resulted in a considerable red-shift ($\lambda_{\text{abs}} = 480$ nm) and broader UV-vis absorption compared with that of DH-BBR⁺Cl⁻ (Figure S7a). DTNPs also showed significantly increased scattering around 500-650 nm, further confirming the formation of nanoparticles in PBS buffer. This red-shift in the UV-vis absorption could be attributed to the J-aggregation of DH-BBR cations in DTNPs, which caused remarkable fluorescence quenching (Figure S7a). The quenched fluorescence could be recovered when DTNPs were degraded in DMSO (Figure S7b). The investigation of stability of DTNPs (20 μ M) in either PBS (1 \times , pH 7.4), serum-PBS (PBS containing 10% mouse serum), or cell culture medium

(DMEM) showed that DTNPs were very stable under physiologically relevant conditions (Figure S8), attributing to the small critical micelle concentration (CMC; 2.86 μ M, Figure S9) and negative zeta potential (-8.5 mV). Moreover, DTNPs were also very stable either in PBS buffer with different pH (5.0-7.4) or in water with the addition of varying NaCl concentrations (Figures S10 & S11).

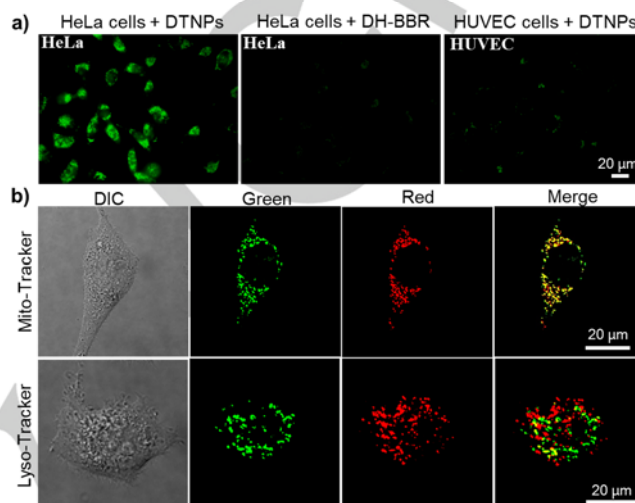


Figure 3. Evaluation of the uptake of DTNPs in cells using fluorescence imaging. (a) Fluorescence imaging of HeLa cells following incubation with DH-BBR (20 μ M), DTNPs (20 μ M), or HUVEC cells incubated with DTNPs (20 μ M) for 2 h. (b) Colocalization studies of HeLa cells following incubation with DTNPs (pseudo green) and the Mito-Tracker Red (pseudo red, up) or Lyso-Tracker Red (pseudo red, down). Cells were incubated with 200 nM the Mito-Tracker Red or Lyso-Tracker Red for 20 min and then incubated with DTNPs (20 μ M) for 1 h. The colocalization of green fluorescence from the DH-BBR⁺ with red fluorescence from the Mito-Tracker Red but not Lyso-Tracker Red suggests that DH-BBR⁺ accumulates mainly in the mitochondria.

The uptake of DTNPs into HeLa tumor cells was then studied after optimizing the incubation conditions. DTNPs could enter into HeLa cells in both incubation concentration- and time-dependent manners (Figure S12), producing bright fluorescence in HeLa cells after incubation with 20 μ M DTNPs for 2 h (Figure 3a). The strong fluorescence was also verified by flow cytometric analysis, revealing that the fluorescence intensity in HeLa cells reached maximum upon incubation with DTNPs (20 μ M) for 2 h (Figure S13). In contrast, the incubation of HeLa cells with DH-BBR⁺Cl⁻ (20 μ M) for 2 h produce much weaker intracellular fluorescence (Figure 3a). We then employed the high performance liquid chromatography (HPLC) assay to quantify the cellular uptake of DH-BBR⁺. We found that the amount of DH-BBR⁺ in each HeLa cell following incubation with 20 μ M DTNPs for 2 h was ~ 4.50 fmol, which was more than 2-fold larger than that with DH-BBR⁺Cl⁻ (~ 1.89 fmol/cell) (Table 1). These results demonstrated that DTNPs had a remarkably improved ability to deliver DH-BBR⁺ into HeLa cells compared to that of DH-BBR⁺Cl⁻. The subsequent colocalization study with either Mito-Tracker Red or Lyso-Tracker Red revealed that the green fluorescence of DH-BBR⁺ overlapped well with the red fluorescence of Mito-Tracker (Figures 3b & S14),

FULL PAPER

suggesting that DH-BBR⁺ was distributed mainly in the mitochondria. It was notable that the DTNPs-induced mitochondrial fluorescence in HeLa cells with S or G₂/M phase arrest was significantly higher than that in G₀/G₁ phase (Figure S15), correlating well to the higher mitochondrial membrane potential ($\Delta\psi_m$) observed in S or G₂/M phase.^[19] These results suggested that DTNPs was able to monitor the changes in mitochondria during cell cycle progression.

Table 1. Quantification of the amount of DH-BBR⁺ in HeLa cells following incubation with DH-BBR⁺Cl⁻ or DTNPs.

Probe	Cellular uptake of DH-BBR ⁺ (fmol/cell) ^a		
	10 μ M, 1 h	10 μ M, 2 h	20 μ M, 2 h
DH-BBR ⁺ Cl ⁻	0.85	1.18	1.89
DTNPs	3.72	3.97	4.50

^a Calculated based on the HPLC assay using a standard curve. HeLa cells ($\sim 1 \times 10^6$) were incubated with DH-BBR⁺Cl⁻ or DTNPs for 1 or 2 h, and then lysed with RIPA buffer. The amount of DH-BBR⁺ in the cell lysates were analyzed by HPLC, and normalized to each cell.

To investigate the mechanism involved in the cellular uptake of DTNPs, we first incubated HeLa cells with 20 μ M DTNPs at 4 $^{\circ}$ C for 2 h. Interestingly, there was little difference in intracellular fluorescence compared with that at 37 $^{\circ}$ C, suggesting that the uptake of DTNPs was not energy-dependent (Figure S16). We then pretreated HeLa cells with different endocytosis inhibitors, such as chlorpromazine (CPZ),^[20] Filipin III,^[21] and 5-(N-ethyl-N-isopropyl) amiloride (EIPA),^[22] which also had little effect on the intracellular fluorescence (Figure S17). These results suggested that the intracellular delivery of DTNPs did not rely on the endocytosis/phagocytosis pathway. Furthermore, HPLC analysis of both culture medium and lysed HeLa cells following incubation with 20 μ M DTNPs for 2 h showed that the majority of cationic DH-BBR⁺ was taken up by HeLa cells, while the anionic TPB⁻ was distributed mainly extracellularly (Figure S 18). Bearing in mind that cancer cell membranes are characterized by negative charges, we proposed that the uptake of DTNPs might be related to an electrostatic interaction-driven anion exchange process (Figure 1b).^[23] When DTNPs arrive at the surface of cell membranes, the hydrophilic anions, such as phosphates, can interact with the DH-BBR⁺ cations in DTNPs and cause nanoparticle degradation. The subsequent anion exchange between the TPB⁻ in DH-BBR⁺TPB⁻ ion-pair and anions on the cell membrane can facilitate DH-BBR⁺ entry into cells, ultimately accumulating in the mitochondria, while the repulsion interaction between membrane-bound anions and TPB⁻ will prevent the uptake of TPB⁻. As such, this process can help to bypass energy-dependent endocytosis, leading to fast and enhanced cellular uptake. Indeed, time-course fluorescence images of live HeLa cells revealed that the fluorescence appeared at cell membranes in only 1 min, and rapidly became brighter in the cytoplasm within 3 min (Figure S19 & Movie S1). In contrast, the intracellular

fluorescence was substantially reduced when free phosphates (10, 20, 40, and 60 mM) were added into the culture medium to outcompete the phosphates on cell membrane (Figure S20), confirming the important roles of cell membrane anions in triggering cellular uptake of DTNPs.

Notably, the incubation of human umbilical vein endothelial cells (HUVEC) with DTNPs showed significantly reduced intracellular fluorescence relative to that of HeLa cells (Figure 3a), indicating less uptake of DTNPs into HUVEC cells. This could be attributed to the fact that normal cells generally possess much fewer anions on their membranes,^[18b,24] thus limiting the proposed electrostatic interaction-driven anion exchange process to induce cellular uptake. Additionally, the relatively less mitochondrial activity in normal cells could also lead to lower intracellular fluorescence.^[25]

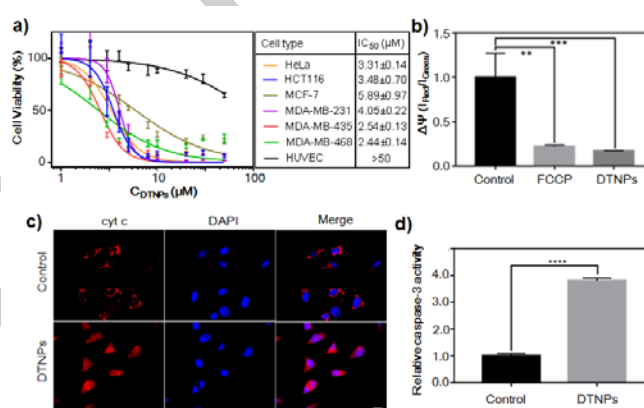


Figure 4. Investigation of the cytotoxicity against tumor cells. (a) Cell viability of indicated cells following incubation with varying concentrations of DTNPs for 48 h. Values were mean \pm SD (n = 3). (b) The quantitative measurement of mitochondrial membrane potential ($\Delta\psi_m$) of HeLa cells using mitochondria staining dye JC-10. HeLa cells were untreated (control), treated with DTNPs (20 μ M) for 4 h or a mitochondria uncoupling agent FCCP (20 μ M) for 30 min, and then incubated with JC-10 (10 μ M) for additional 20 min. The intensities of green fluorescence (I_{Green} , monomer of JC-10) and red fluorescence (I_{Red} , aggregate of JC-10) were measured on a microplate reader, respectively. The $\Delta\psi_m$ was obtained from the $I_{\text{Red}}/I_{\text{Green}}$, and normalized to the control HeLa cells. Values were mean \pm SD (n = 3, **P < 0.01, ***P < 0.001). (c) Immunostaining of cyt c in untreated HeLa cells (control) or HeLa cells treated with DTNPs (20 μ M) for 6 h. Scale bar: 20 μ m. (d) Comparison of the relative caspase-3 activity in untreated HeLa cells (control) or HeLa cells following treatment with DTNPs (20 μ M) for 6 h. Values were mean \pm SD (n = 3, ****P < 0.0001).

The cytotoxicity of DTNPs toward both tumor cells and normal cells was then evaluated using the MTT assay. As shown in Figure 4a, DTNPs exhibited high cytotoxicity against all the six tested tumor cells, including HeLa, HCT116, MCF-7, MDA-MB-231, MDA-MB-435, and MDA-MB-468 cells, with IC₅₀ values of ~ 3.31 , 3.48, 5.89, 4.05, 2.54, and 2.44 μ M, respectively. The IC₅₀ value of DTNPs toward MDA-MB-231 cells was approximately 8-fold smaller than that of DH-BBR⁺Cl⁻ (~ 32.87 μ M), while Na⁺TPB⁻ alone showed almost no cytotoxicity (Figure S21). These results suggested that the cation DH-BBR⁺ and anion TPB⁻ combination played a synergistic role in tuning the cytotoxicity against tumor cells. In contrast, DTNPs showed much lower cytotoxicity against

FULL PAPER

HUVECs cells, with more than 60% cells remaining alive after incubation with DTNPs (50 μM) for 48 h (Figure 4a), consistent with their reduced uptake in HUVEC cells (Figure 3a).

We next investigated the potential mechanism of DTNPs to induce tumor cell death. We found that the fluorescence of DTNPs in HeLa cells was significantly reduced when the incubation was prolonged over 4 h (Figures S12a & S13), which was also observed when HeLa cells were pretreated with a mitochondrial uncoupling agent *p*-trifluoromethoxyphenylhydrazone (FCCP) (Figure S22). The reduced fluorescence could be attributed to the decline of membrane potential in mitochondria, which was confirmed by the subsequent measurement of the $\Delta\psi_m$ with a commercial JC-10 dye. It was revealed that DTNPs could apparently reduce the $\Delta\psi_m$ to a level similar to that induced by FCCP (Figures 4b & S23). In addition, immunostaining of cyt c in DTNPs-treated HeLa cells showed an obvious distribution of cyt c in the cytosol, different to that observed in non-treated viable cells, in which the cyt c was distributed mainly in the mitochondria (Figure 4c). These results suggested that the selective accumulation of cation DH-BBR⁺ from DTNPs in the mitochondria of cancer cells could efficiently trigger mitochondrial dysfunctions, resulting in the release of DH-BBR⁺ and cyt c to cytosol. As cyt c is a proapoptotic inducer that can activate caspase cascades and induce cell apoptosis,^[26] caspase-3 activity and apoptosis events in DTNP-treated HeLa cells were next examined. The results in Figure 4d showed that the caspase-3 activity in HeLa cells was significantly increased upon treatment with DTNPs, which could trigger significant cell apoptosis, as revealed by the flow cytometric analysis of DTNPs-treated HeLa cells with Annexin V/propidium iodide (PI) staining (Figure S24). These results demonstrated that DTNPs could induce severe cell death through a mitochondria-dependent apoptosis pathway.

injection, once every two days for a total of ten times. As shown in Figure 5a, the tumor volumes in the mice receiving i.v. injection of DTNPs (10 mg/kg) were significantly reduced compared with those receiving either DH-BBR (10 mg/kg) or saline as the control. The average tumor volume in the DTNPs-treated mice at day 20 was ~58% smaller than that treated with saline (~5-fold vs ~12-fold). Mice treated with DTNPs did not show an obvious change in body weight compared with those treated with saline, implying minimal side effects of DTNPs in the mice (Figure 5b). The significant difference in tumor size was also confirmed by photograph of tumors resected from mice after treatment for 20 days (Figure 5c). Hematoxylin-eosin (H&E) and terminal deoxynucleotidyl transferase dUTP nick end labeling (TUNEL) staining of tumor tissue slices resected from DTNPs-treated mice showed significant cell death and apoptosis in the tumor tissues, while tumor tissues resected from saline-treated mice showed negligible cell death and apoptosis (Figures 5d & 5e). The obvious tumor cell apoptosis could be attributed to the efficient uptake of DTNPs into tumors, which was revealed by the remarkable fluorescence in DTNPs-treated tumor tissues (Figure 5f). These results indicated that DTNPs assembled from the DH-BBR·TPB ion-pair were able to efficiently enter into tumors and inhibit tumor growth in living mice. To the best of our knowledge, this is the first time to show the *in vivo* antitumor activity of BBR-based compounds. However, Figure 5a also showed that the tumor remained growing during the course of therapy with DTNPs, albeit the growth rate was significantly reduced. It is still very challenging to eliminate the tumors *in vivo* using DTNPs only. In future, a combination chemotherapy with DTNPs and immunotherapy with antibodies (e.g., Anti-PD-L1, vaccines)^[27] may largely improve the therapeutic effect against cancers.

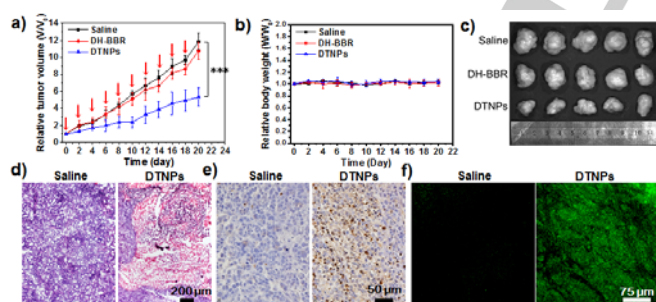


Figure 5. Antitumor efficiency of DTNPs *in vivo*. (a,b) The change of tumor volumes (a) and body weight (b) of HeLa tumor-bearing nude mice following i.v. injection with saline, 10 mg/kg DH-BBR or 10 mg/kg DTNPs for 20 days. Values were mean \pm SD ($n = 5$, *** $P < 0.001$). Red arrows in (a) indicated injection days. (c) Photograph of HeLa tumors resected from mice after indicated treatment at day 20. (d,e,f) H&E staining (d), TUNEL staining (e) and fluorescence imaging (f) of tumor tissue slices resected from HeLa tumor-bearing mice following treatment with saline or DTNPs. The mice were treated with saline or DTNPs (10 mg/kg) every other day, and last for 20 days. The tumors were resected from mice on day 20.

Encouraged by the enhanced cellular uptake and cytotoxicity, we next examined the antitumor activity in nude mice bearing subcutaneous HeLa tumors. Mice were administered with saline, DH-BBR⁺Cl⁻ or DTNPs (10 mg/kg) in saline through intravenous

Conclusions

In conclusion, we report the study of using a lipophilic anion TPB-driven self-assembly of a novel mitochondria targeting fluorescent compound, DH-BBR, into organic nanoparticles DTNPs for cell imaging and improved antitumor efficacy. We employed X-ray crystallography to reveal that the formation of DTNPs was caused by a synergy of strong molecular interactions, including π - π stacking, $O \cdots \pi$ interaction and electrostatic interaction. The subsequent fluorescence imaging showed that DTNPs could remarkably enhance the uptake of DH-BBR into tumor cells through an electrostatic interaction-mediated anion exchange process, inducing significant mitochondrial dysfunction and cell apoptosis. Moreover, DTNPs could enhance the delivery of DH-BBR into tumors following i.v. administration, resulting in efficient inhibition of tumor growth with negligible side effects in living mice. The results reported here revealed that the use of lipophilic anions to trigger self-assembly of DH-BBR into nanoparticles was promising for cancer treatment, which could serve as a general approach to enhance the delivery of DLC-based small molecules into tumors, thus improving antitumor efficacy.

FULL PAPER

Experimental Section

General Materials and Methods. All chemicals and biological reagents were purchased from commercial suppliers and used without further purification. Analytical thin-layer chromatography (TLC) was HSGF 254 (150–200 μm thickness, Yantai Huiyou Company, China). Nuclear magnetic resonance (NMR) spectra were performed on a Bruker AMX-400 and AMX-500 NMR. Chemical shifts were reported in parts per million (ppm, δ) downfield from tetramethylsilane (TMS). Proton coupling patterns were described as singlet (s), doublet (d), triplet (t), quartet (q), multiplet (m) and broad (br). Low- and high-resolution mass spectra (MS and HRMS) were given with electrospray ionization (ESI) and electric ionization (EI) produced by Finnigan MAT-95. Single crystal x-ray diffraction data were collected using Bruker-AXS SMART-APEXII CCD diffractometer. HPLC analysis was conducted on Thermo Fisher U3000 HPLC systems. Absorption spectra were recorded on an Ocean Optics UV-vis spectrometer. Fluorescence spectra were collected on a HORIBA Jobin Yvon Fluoromax-4 fluorescence spectrometer. Absolute quantum yield was measured by calibrated integrating sphere system (Integrating Sphere F-3018, HORIBA Jobin Yvon). Fluorescence imaging assays were conducted on a Leica SP5 confocal laser scanning microscope or an Olympus IX73 fluorescent inverted microscope. Dynamic light scattering analysis and Zeta potential analysis were conducted on a 90 Plus/ BI-MAS equipment (Brookhaven, USA). Flow cytometric analysis was conducted on a Coulter FC-500 flow cytometer (Beckman Coulter, USA). MTT assay was performed on a microplate reader (Tcan). The in vivo MR imaging experiments were performed on a 1.0 T small animal MRI system (Bruker ICON).

Synthesis. DH-BBR and DH-BBR-TPB were synthesized according to the procedure in Schemes S1 and S2. The structure characterizations of them were described in the Supporting Information.

Single crystal structure determination. The crystal of DH-BBR-TPB was obtained by slow evaporation of the $\text{CH}_3\text{OH}-\text{CH}_2\text{Cl}_2$ solution of DH-BBR-TPB at r.t.. A single crystal with dimensions of $0.12 \times 0.1 \times 0.1 \text{ mm}^3$ was used for structural determination, and the structure refinement data were collected on a Bruker-AXS SMART-APEXII CCD diffractometer using graphite-monochromated Mo K radiation ($\lambda = 0.71073 \text{ \AA}$) at room temperature. The crystallographic data for complex DH-BBR-TPB are listed in Table S3. The refinement details could be found in the cif file (CCDC 1588249) of DH-BBR-TPB, which are provided free of charge by The Cambridge Crystallographic Data Centre via www.ccdc.cam.ac.uk/data_request/cif.

Cell cultures. HeLa, HCT116, MCF-7, MDA-MB-213, MDA-MB-435 and MDA-MB-468 tumor cells were grown in high glucose DMEM medium (Gibco) supplemented with 10% (v/v) fetal bovine serum (FBS) and 1% (v/v) penicillin/streptomycin (PS). All cells were cultured in a 5% CO_2 humidified incubator at 37 $^\circ\text{C}$.

Fluorescence imaging and colocalization analysis. HeLa cells ($\sim 5 \times 10^4$) were seeded to a glass-bottom cell culture dish, and kept growing overnight. Varying concentrations of BBR, DH-BBR or DTNPs (5, 10, 20 μM) in FBS free DMEM medium were added into cells and incubated at 37 $^\circ\text{C}$ for 10 min, 0.5, 1, 2, 4 and 6 h. After incubation, the medium was removed and the cells were washed with cold PBS for three times. Fluorescence images were then acquired using an Olympus IX73 fluorescent inverted microscope.

For Co-localization studies, HeLa cells were incubated with 200 nM MitoTracker (MitoTrackerTM Red CMXRos) or LysoTracker (LysoTrackerTM Red DND-99) for 20 min. After being washed with cold

PBS for three times, the cells were then incubated with 20 μM DH-BBR or DTNPs for another 1 h. The fluorescence images of the cells were captured on the fluorescent microscope.

Cytotoxicity assay (MTT). The cells were seeded in flat-bottomed 96-well plates (5000 cells/well) and incubated at 37 $^\circ\text{C}$ for 24 h. Varying concentration of BBR, DH-BBR or DTNPs in DMEM medium were then added. After being incubation for 48 h, 50 μL MTT solution (1 in PBS) was then added into each well. The cells were kept at 37 $^\circ\text{C}$ for 4 h, and the solution in each well was then removed carefully. The resulting purple formazan crystals in the wells were dissolved by addition of 100 μL DMSO. The absorbance (OD) at 550 nm in each well was acquired on a microplate reader (Tcan). The absorbance of blank cells (OD control) were used as the control, and the percentage of cell viability in each treatment was calculated by dividing OD to OD control.

Flow cytometry analysis. Approximately 1×10^6 HeLa cells in 2 mL DMEM medium were seeded onto 6-well plates. After being incubation at 37 $^\circ\text{C}$ overnight, the medium was replaced with 1 mL of fresh medium containing 20 μM DTNPs, and the cells were incubated for 10 min, 0.5, 1, 2, 4 and 6 h. After being washed with PBS ($\times 1$) for three times, trypsin (300 μL) was added into each well, and kept at 37 $^\circ\text{C}$ for 5–10 min to detach the cells. The cell pellets were then collected after centrifugation at 1000 rpm at 4 $^\circ\text{C}$ for 4 min. After being washed with cold PBS buffer, the cell pellets were resuspended in 1 mL cold PBS, and the flow cytometry analysis was conducted on a Beckman FC500 flow cytometer with excitation at 488 nm. For each analysis, 10000 cells were used.

Quantitative analysis of DH-BBR in HeLa cells. Approximately 1×10^6 HeLa cells in 2 mL DMEM medium were seeded onto 6-well plates. After being incubation at 37 $^\circ\text{C}$ overnight, the medium was replaced with 1 mL fresh DMEM containing 10 or 20 μM DH-BBR or DTNPs. The cells were incubated for 1 or 2 h. Then, the medium was carefully removed and the cells were washed with cold PBS three times. The cells were trypsinized, collected, and the cell number were counted. After being lysed with 50 μL RIPA (Radio-Immunoprecipitation Assay) buffer, the cell lysates were collected, mixed with 100 μL cold MeOH, and centrifuged at $14,000 \times g$ at 4 $^\circ\text{C}$ for 10 min. The supernatant was collected, and then injected into an HPLC system for analysis. The amount of DH-BBR in each well was then measured using the standard curve of DH-BBR, with results summarized in Table 1 and Figure S15.

Mitochondrial membrane potential assay. HeLa cells ($\sim 5 \times 10^4$) were seeded to a glass-bottom cell culture dish, and kept growing overnight. DTNPs (20 μM) or FCCP (20 μM) in FBS free medium were then added, and the cells were kept incubation at 37 $^\circ\text{C}$ for 4 h for DTNPs or 30 min for FCCP. After removal of the medium, the cells were washed with cold PBS three times. The mitochondria staining dye JC-10 (10 μM) in fresh medium was then added, and the cells were kept incubation for additional 20 min. Then, the medium was removed, and the cells was washed with cold PBS buffer for three times. The fluorescence images of cells were then acquired on a Leica TCS SP5 confocal laser scanning microscope. A green laser (488 nm) with the emission filter from 500–540 nm was used to detect the green fluorescence of the monomer of JC-10 dye, and a yellow-green laser (543 nm) with the emission filter from 570–650 nm was used to detect the red fluorescence of the aggregates of JC-10 dye. In addition, the mitochondrial membrane potential was measured using a microplate assay. HeLa cells were seeded in 96-well plates with a cell density of 1×10^4 cells per well. After being incubation at 37 $^\circ\text{C}$ overnight, cells were then incubated with FCCP (20 μM) for 30 min or DTNPs (20 μM) for 4 h. After removal of the medium, the cells were washed with cold PBS three times. JC-10 (10 μM) in fresh medium was then added, and the cells were kept incubation for additional 20 min. Then, the medium was removed, and the cells were washed with cold PBS buffer for three times. Both the monomer

FULL PAPER

and aggregates of JC-10 in each well were measured on a Tecan microplate reader. The green fluorescence of JC-10 (monomer) at 535 nm was measured with excitation at 485 nm, and the red fluorescence JC-10 (aggregates) at 596 nm was measured with excitation at 540 nm. The aggregate/monomer ratio in each well was calculated and used to determine the mitochondrial membrane potential $\Delta\psi_m$. Each measurement was repeated for three times, and the data were expressed as mean \pm standard deviation (SD).

Immunofluorescence staining of cyt c. Immunofluorescence staining of cyt c was performed using a recombinant rabbit monoclonal anti-cyt c primary antibody and an Alexa Fluor 594-conjugated donkey anti-rabbit secondary antibody (abcam) according to the protocol described by the manufacture. Briefly, HeLa cells were treated with 20 μ M DTNPs for 6 h, fixed by polyformaldehyde, followed by staining with anti-cyt c primary antibody and secondary antibody. After being staining, the nucleus was further stained with DAPI, and the fluorescence images were then acquired.

Measurement of Caspase-3 activity. HeLa cells were seeded in 96-well plates with a cell density of 1×10^4 cells per well, and incubated at 37 $^{\circ}$ C overnight. Then, the culture medium was replaced with 100 μ L FBS free medium containing 20 μ M DTNPs. After incubation at 37 $^{\circ}$ C for 6 h, the caspase-3 activity in each well was measured using the Caspase-Glo[®] 3 assay (Promega) according to the standard protocol described by the manufacture. Briefly, 100 μ L of Caspase-Glo[®] 3 reagent was added to each well. The plate was then gently mixed, and incubated under dark at r.t. for 30 min. The resulting luminescence was then measured on a Tecan microplate reader. Data were then background-corrected, normalized, and the caspase-3 activity was expressed as normalized increased fold of luminescence intensity compared to the untreated control cells.

Endocytosis inhibition studies. The inhibitors (chlorpromazine (CPZ) for clathrin-mediated endocytosis, filipin III for caveolae-mediated endocytosis and ethylisopropyl amiloride (EIPA) for micropinocytosis) that function at different endocytotic processes were used to determine the possible pathways of cellular uptake. The HeLa cells were treated with or without each inhibitor (30 μ M CPZ, 5 μ g/mL filipin III or 100 μ M EIPA) for 30 min, and then treated with DTNPs (20 μ M) for another 2 h. After being washed with cold PBS three times, the fluorescence images were acquired using a fluorescence microscope. The resulting intracellular fluorescence were quantified for the comparison.

Evaluation of antitumor activity in living mice. Animal care and euthanasia were carried out with the approval of the institutional animal-use and -care regulations of the Model Animal Research Center of Nanjing University (MARC). Six-week-old female nude mice were injected subcutaneously with 4×10^6 HeLa cells to establish xenograft HeLa tumors in the right forelimb axilla. The tumors were allowed to grow to a mean volume of ~ 250 mm³ for the antitumor activity studies. The mice were divided into three groups randomly ($n = 5$). Mice were administered intravenously with saline, 10 mg/kg DH-BBR or 10 mg/kg DTNPs every other day, and last for 20 days. The tumor volume and body weight for each mouse were measured in every other day. The tumor volume was calculated as (tumor length) \times (tumor width)²/2, and the relative tumor volumes were calculated as V/V_0 (V_0 was the tumor volume when the treatment was initiated).

Histopathology evaluation of tumor tissues. After treatment on day 20, the mice were sacrificed and the tumors were resected. After photograph, the tumors were frozen in optimal cutting temperature medium (OCT) and cut into 10 μ m thick slices using a vibrating-blade microtome. The fluorescence images of the tumor tissue slices were then acquired on a Leica TCS SP5 confocal laser scanning microscope. For H&E staining and TUNEL staining, tumors were fixed in formalin. Then, the tumors were

sectioned into 10- μ m slices. The H&E staining and TUNEL staining were performed according to the manufacturer's instructions (KeyGen Biotech. Co. Ltd., Nanjing, China). The images were acquired on an IX73 optical microscope equipped with a color camera.

Statistical analysis. Statistical comparisons between two groups were determined by Student's t-test. $p < 0.05$ was considered to be statistical significance. The statistical tests were run with Prism 6 (Prism GraphPad Software, Inc., San Diego).

Acknowledgements

We gratefully acknowledge financial support from the National Natural Science Foundation of China (81620108027, 21632008, 21775071, 91229204 and 81220108025), the Major Project of Chinese National Programs for Fundamental Research and Development (2015CB910304) and National S&T Major Projects (2014ZX09507002-001).

Keywords: self-assembly • dehydroberberine • mitochondria • cell imaging • antitumor

- [1] a) G. Liang, H. Ren, J. Rao, *Nat. Chem.* **2010**, *2*, 54-60; b) Y. Gao, J. Shi, D. Yuan, B. Xu, *Nat. Commun.* **2012**, *3*, 1033; c) D. Ye, A. J. Shuhendler, L. Cui, L. Tong, S. S. Tee, G. Tikhomirov, D. W. Felsher, J. Rao, *Nat. Chem.* **2014**, *6*, 519-526; d) Y. Yuan, S. Ge, H. Sun, X. Dong, H. Zhao, L. An, J. Zhang, J. Wang, B. Hu, G. Liang, *ACS Nano* **2015**, *9*, 5117-5124; e) D. Zhang, G. B. Qi, Y. X. Zhao, S. L. Qiao, C. Yang, H. Wang, *Adv. Mater.* **2015**, *27*, 6125-6130.
- [2] a) A. G. Cheetham, P. Zhang, Y. A. Lin, L. L. Lock, H. Cui, *J. Am. Chem. Soc.* **2013**, *135*, 2907-2910; b) P. Huang, D. Wang, Y. Su, W. Huang, Y. Zhou, D. Cui, X. Zhu, D. Yan, *J. Am. Chem. Soc.* **2014**, *136*, 11748-11756; c) Y. Yuan, L. Wang, W. Du, Z. Ding, J. Zhang, T. Han, L. An, H. Zhang, G. Liang, *Angew. Chem. Int. Ed.* **2015**, *54*, 9700-9704; d) J. Zhang, Y. C. Liang, X. Lin, X. Zhu, L. Yan, S. Li, X. Yang, G. Zhu, A. L. Rogach, P. K. Yu, P. Shi, L. C. Tu, C. C. Chang, X. Zhang, X. Chen, W. Zhang, C. S. Lee, *ACS Nano* **2015**, *9*, 9741-9756; e) Y. Cai, H. Shen, J. Zhan, M. Lin, L. Dai, C. Ren, Y. Shi, J. Liu, J. Gao, Z. Yang, *J. Am. Chem. Soc.* **2017**, *139*, 2876-2879; f) A. G. Cheetham, R. W. Chakraborty, W. Ma, H. Cui, *Chem. Soc. Rev.* **2017**, *46*, 6638-6663; g) Z. Zhang, L. Shi, C. Wu, Y. Su, J. Qian, H. Deng, X. Zhu, *ACS Appl. Mater. Interfaces* **2017**, *9*, 29505-29514.
- [3] a) Y. Kuang, B. Xu, *Angew. Chem. Int. Ed.* **2013**, *52*, 6944-6948; b) J. Shi, B. Xu, *Nano Today* **2015**, *10*, 615-630; c) Y. Huang, G. Zhang, F. Hu, Y. Jin, R. Zhao, D. Zhang, *Chem. Sci.* **2016**, *7*, 7013-7019; d) Y. Wen, W. Zhang, N. Gong, Y. F. Wang, H. B. Guo, W. Guo, P. C. Wang, X. J. Liang, *Nanoscale* **2017**, *9*, 14347-14356.
- [4] a) L. Adler-Abramovich, L. Vaks, O. Carny, D. Trudler, A. Magno, A. Cafilisch, D. Frenkel, E. Gazit, *Nat. Chem. Biol.* **2012**, *8*, 701-706; b) F. Clerici, E. Erba, M. L. Gelmi, S. Pellegrino, *Tetrahedron Lett.* **2016**, *57*, 5540-5550; c) K. Tao, A. Levin, L. Adler-Abramovich, E. Gazit, *Chem. Soc. Rev.* **2016**, *45*, 3935-3953.
- [5] a) E. De Santis, M. G. Ryadnov, *Chem. Soc. Rev.* **2015**, *44*, 8288-8300; b) K. Liu, R. Xing, Q. Zou, G. Ma, H. Mohwald, X. Yan, *Angew. Chem. Int. Ed.* **2016**, *55*, 3036-3039; c) M. Abbas, Q. Zou, S. Li, X. Yan, *Adv. Mater.* **2017**, *29*, 1605021.
- [6] a) J. F. Lovell, C. S. Jin, E. Huynh, H. Jin, C. Kim, J. L. Rubinstein, W. C. Chan, W. Cao, L. V. Wang, G. Zheng, *Nat. Mater.* **2011**, *10*, 324-332; b) D. Ye, G. Liang, M. L. Ma, J. Rao, *Angew. Chem. Int. Ed.* **2011**, *50*, 2275-2279; c) J. Wang, F. Chen, S. J. Arconada-Alvarez, J. Hartanto, L. P. Yap, R. Park, F. Wang, I. Vorobyova, G.

FULL PAPER

- Dagliyan, P. S. Conti, J. V. Jokerst, *Nano Lett.* **2016**, *16*, 6265-6271;
- d) M. Zheng, Y. Wang, H. Shi, Y. Hu, L. Feng, Z. Luo, M. Zhou, J. He, Z. Zhou, Y. Zhang, D. Ye, *ACS Nano* **2016**, *10*, 10075-10085;
- e) Y. Cai, P. Liang, Q. Tang, X. Yang, W. Si, W. Huang, Q. Zhang, X. Dong, *ACS Nano* **2017**, *11*, 1054-1063; f) Q. Zou, M. Abbas, L. Zhao, S. Li, G. Shen, X. Yan, *J. Am. Chem. Soc.* **2017**, *139*, 1921-1927; g) J. Wang, C. Y. Lin, C. Moore, A. Jhunjhunwala, J. V. Jokerst, *Langmuir* **2018**, *34*, 359-365.
- [7] a) D. Ye, A. J. Shuhendler, P. Pandit, K. D. Brewer, S. S. Tee, L. Cui, G. Tikhomirov, B. Rutt, J. Rao, *Chem. Sci.* **2014**, *4*, 3845-3852; b) Y. Yuan, F. Wang, W. Tang, Z. Ding, L. Wang, L. Liang, Z. Zheng, H. Zhang, G. Liang, *ACS Nano* **2016**, *10*, 7147-7153.
- [8] a) J. Li, Y. Kuang, J. Shi, J. Zhou, J. E. Medina, R. Zhou, D. Yuan, C. Yang, H. Wang, Z. Yang, J. Liu, D. M. Dinulescu, B. Xu, *Angew. Chem. Int. Ed.* **2015**, *54*, 13307-13311; b) H. Wang, Z. Feng, D. Wu, K. J. Fritzsche, M. Rigney, J. Zhou, Y. Jiang, K. Schmidt-Rohr, B. Xu, *J. Am. Chem. Soc.* **2016**, *138*, 10758-10761; c) P. K. Magut, S. Das, V. E. Fernand, J. Losso, K. McDonough, B. M. Naylor, S. Aggarwal, I. M. Warner, *J. Am. Chem. Soc.* **2013**, *135*, 15873-15879.
- [9] a) Z. Feng, H. Wang, R. Zhou, J. Li, B. Xu, *J. Am. Chem. Soc.* **2017**, *139*, 3950-3953; b) L. L. Li, S. L. Qiao, W. J. Liu, Y. Ma, D. Wan, J. Pan, H. Wang, *Nat. Commun.* **2017**, *8*, 1276.
- [10] a) A. Shao, Y. Xie, S. Zhu, Z. Guo, S. Zhu, J. Guo, P. Shi, T. D. James, H. Tian, W. H. Zhu, *Angew. Chem. Int. Ed.* **2015**, *54*, 7275-7280; b) S. R. MacEwan, A. Chilkoti, *Angew. Chem. Int. Ed.* **2017**, *56*, 6712-6733.
- [11] a) S. Karnewar, S. B. Vasamsetti, R. Gopaju, A. K. Kanugula, S. K. Ganji, S. Prabhakar, N. Rangaraj, N. Tupperwar, J. M. Kumar, S. Kotamraju, *Sci. Rep.* **2016**, *6*, 24108; b) C. J. Zhang, J. Wang, J. Zhang, Y. M. Lee, G. Feng, T. K. Lim, H. M. Shen, Q. Lin, B. Liu, *Angew. Chem. Int. Ed.* **2016**, *55*, 13770-13774.
- [12] N. Yang, M. Weinfeld, H. Lemieux, B. Montpetit, I. S. Goping, *Cell Death Dis.* **2017**, *8*, e2587.
- [13] J. Zielonka, J. Joseph, A. Sikora, M. Hardy, O. Ouari, J. Vasquez-Vivar, G. Cheng, M. Lopez, B. Kalyanaraman, *Chem. Rev.* **2017**, *117*, 10043-10120.
- [14] a) X. Zhang, Q. Ba, Z. Gu, D. Guo, Y. Zhou, Y. Xu, H. Wang, D. Ye, H. Liu, *Chem. Eur. J.* **2015**, *21*, 17415-17421; b) A. Kurutos, I. Orehovec, A. Tomašić Pačić, I. Crnolatac, L. Horvat, N. Gadjević, I. Piantanida, T. Deligeorgiev, *Dyes and Pigments* **2018**, *148*, 452-459.
- [15] S. Luo, X. Tan, S. Fang, Y. Wang, T. Liu, X. Wang, Y. Yuan, H. Sun, Q. Qi, C. Shi, *Adv. Funct. Mater.* **2016**, *26*, 2826-2835.
- [16] a) N. Luiza Andreazza, C. Vevert-Bizet, G. Bourg-Heckly, F. Sureau, M. Jose Salvador, S. Bonneau, *Int. J. Pharm.* **2016**, *510*, 240-249;
- b) L. Zhang, X. J. Miao, X. Wang, H. H. Pan, P. Li, H. Ren, Y. R. Jia, C. Lu, H. B. Wang, L. Yuan, G. L. Zhang, *Sci. Rep.* **2016**, *6*, 28116.
- [17] a) G. C. Pereira, A. F. Branco, J. A. Matos, S. L. Pereira, D. Parke, E. L. Perkins, T. L. Serafim, V. A. Sardao, M. S. Santos, A. J. Moreno, J. Holy, P. J. Oliveira, *J. Pharmacol. Exp. Ther.* **2007**, *323*, 636-649; b) K. N. Chidambara Murthy, G. K. Jayaprakasha, B. S. Patil, *Eur. J. Pharmacol.* **2012**, *688*, 14-21.
- [18] a) M. Yang, W. J. Brackenbury, *Front. Physiol.* **2013**, *4*, 185; b) B. Chen, W. Le, Y. Wang, Z. Li, D. Wang, L. Lin, S. Cui, J. J. Hu, Y. Hu, P. Yang, R. C. Ewing, D. Shi, Z. Cui, *Theranostics* **2016**, *6*, 1887-1898.
- [19] M. Martínez-Diez, G. Santamaría, Á. D. Ortega, J. M. Cuezva, *Plos One* **2006**, *1*, e107.
- [20] C. Dalal, A. Saha, N. R. Jana, *J. Phys. Chem. C* **2016**, *120*, 6778-6786.
- [21] J. V. Georgieva, D. Kalicharan, P. O. Couraud, I. A. Romero, B. Weksler, D. Hoekstra, I. S. Zuhorn, *Mol. Ther.* **2011**, *19*, 318-325.
- [22] N. K. Y. Wong, R. A. Sheno, S. Abbina, I. Chafeeva, J. N. Kizhakkedathu, M. K. Khan, *Biomacromolecules* **2017**, *18*, 2427-2438.
- [23] a) N. Chuard, K. Fujisawa, P. Morelli, J. Saabach, N. Winssinger, P. Metrangolo, G. Resnati, N. Sakai, S. Matile, *J. Am. Chem. Soc.* **2016**, *138*, 11264-11271; b) D. Sobot, S. Mura, P. Couvreur, *J. Mater. Chem. B* **2016**, *4*, 5078-5100.
- [24] a) E. Hondroulis, R. Zhang, C. Zhang, C. Chen, K. Ino, T. Matsue, C. Z. Li, *Theranostics* **2014**, *4*, 919-930; b) C. Gui, E. Zhao, R. T. K. Kwok, A. C. S. Leung, J. W. Y. Lam, M. Jiang, H. Deng, Y. Cai, W. Zhang, H. Su, B. Z. Tang, *Chem. Sci.* **2017**, *8*, 1822-1830.
- [25] a) V. R. Fantin, P. Leder, *Cancer Res.* **2004**, *64*, 329-336; b) S. Wu, Q. Cao, X. Wang, K. Cheng, Z. Cheng, *Chem. Commun.* **2014**, *50*, 8919-8922.
- [26] a) M. E. Fitch, C. M. Chang, T. G. Parslow, *Cell Death Differ.* **2000**, *7*, 338-349; b) M. A. McDonnell, D. Wang, S. M. Khan, M. G. Vander Heiden, A. Kelekar, *Cell Death Differ.* **2003**, *10*, 1005-1015.
- [27] a) J. Bellmunt, T. Powles, N. J. Vogelzang, *Cancer Treat. Rev.* **2017**, *54*, 58-67; b) H. Cai, Z.-H. Huang, L. Shi, Y.-F. Zhao, H. Kunz, Y.-M. Li, *Chem. Eur. J.* **2011**, *17*, 6396-6406; c) C. H. Marzabadi, R. W. Franck, *Chem. Eur. J.* **2016**, *23*, 1728-1742.

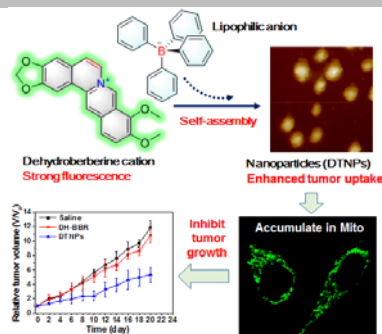
FULL PAPER

Entry for the Table of Contents (Please choose one layout)

Layout 1:

FULL PAPER

Lipophilic anion-driven self-assembly of fluorescent mitochondria-targeting dehydroberberine into organic nanoparticles is demonstrated for fluorescence imaging of tumor cells and inhibition of tumor growth in mice.



Ruibing An, Zhanni Gu, Haifeng Sun, Yuxuan Hu, Runqi Yan, Deju Ye,* and Hong Liu,*

Page No. – Page No.

Self-assembly of Fluorescent
Dehydroberberine Enhances
Mitochondria-Dependent Antitumor
Efficacy